




Article

Role of MRI-Derived Radiomics Features in Determining Degree of Tumor Differentiation of Hepatocellular Carcinoma

Sanaz Ameli ¹, Bharath Ambale Venkatesh ² , Mohammadreza Shaghghi ², Maryam Ghadimi ², Bita Hazhirkarzar ², Roya Rezvani Habibabadi ³, Mounes Aliyari Ghasabeh ⁴, Pegah Khoshpouri ⁵ , Ankur Pandey ⁶, Pallavi Pandey ², Li Pan ², Robert Grimm ² and Ihab R. Kamel ^{2,*} 

¹ Department of Radiology, University of Arkansas for Medical Sciences, 4301 W. Markham St., Little Rock, AR 72205, USA

² Department of Radiology, Johns Hopkins Hospital, 600 N Wolfe St., Baltimore, MD 21287, USA

³ Department of Radiology, University of Florida College of Medicine, 1600 SW Archer Rd., Gainesville, FL 32610, USA

⁴ Department of Radiology, Saint Louis University, 1201 S Grand Blvd., St. Louis, MO 63104, USA

⁵ Department of Radiology, University of Washington Main Hospital, 1959 NE Pacific St., 2nd Floor, Seattle, WA 98195, USA

⁶ Department of Radiology, University of Maryland Medical Center, 22 S Greene St., Baltimore, MD 21201, USA

* Correspondence: ikamel@jhmi.edu



Citation: Ameli, S.; Venkatesh, B.A.; Shaghghi, M.; Ghadimi, M.; Hazhirkarzar, B.; Rezvani Habibabadi, R.; Aliyari Ghasabeh, M.; Khoshpouri, P.; Pandey, A.; Pandey, P.; et al. Role of MRI-Derived Radiomics Features in Determining Degree of Tumor Differentiation of Hepatocellular Carcinoma. *Diagnostics* **2022**, *12*, 2386. <https://doi.org/10.3390/diagnostics12102386>

Academic Editor: Bin Song

Received: 22 August 2022

Accepted: 26 September 2022

Published: 30 September 2022

Publisher's Note: MDPI stays neutral with regard to jurisdictional claims in published maps and institutional affiliations.



Copyright: © 2022 by the authors. Licensee MDPI, Basel, Switzerland. This article is an open access article distributed under the terms and conditions of the Creative Commons Attribution (CC BY) license (<https://creativecommons.org/licenses/by/4.0/>).

Abstract: **Background:** To investigate radiomics ability in predicting hepatocellular carcinoma histological degree of differentiation by using volumetric MR imaging parameters. **Methods:** Volumetric venous enhancement and apparent diffusion coefficient were calculated on baseline MRI of 171 lesions. Ninety-five radiomics features were extracted, then random forest classification identified the performance of the texture features in classifying tumor degree of differentiation based on their histopathological features. The Gini index was used for split criterion, and the random forest was optimized to have a minimum of nine participants per leaf node. Predictor importance was estimated based on the minimal depth of the maximal subtree. **Results:** Out of 95 radiomics features, four top performers were apparent diffusion coefficient (ADC) features. The mean ADC and venous enhancement map alone had an overall error rate of 39.8%. The error decreased to 32.8% with the addition of the radiomics features in the multi-class model. The area under the receiver-operator curve (AUC) improved from 75.2% to 83.2% with the addition of the radiomics features for distinguishing well-from moderately/poorly differentiated HCCs in the multi-class model. **Conclusions:** The addition of radiomics-based texture analysis improved classification over that of ADC or venous enhancement values alone. Radiomics help us move closer to non-invasive histologic tumor grading of HCC.

Keywords: carcinoma; hepatocellular; machine learning; neoplasm grading; diffusion magnetic resonance imaging; contrast media

1. Introduction

Hepatocellular carcinoma (HCC) is among the most common causes of cancer in the world, and with an increase in its incidence, it now became the second most common cause of cancer-related mortality worldwide [1]. Despite the new surgical and chemotherapeutic techniques in treating HCC tumors, treatment outcome is still suboptimal. Several studies have shown that HCC tumors' histological grade is one of the critical factors in determining treatment outcome and patients' overall survival [2]. For this reason, determining the degree of differentiation in HCC tumors at presentation can help practitioners to make an optimal treatment strategy and predict the outcomes more accurately [3]. The characteristic features of HCC on contrast-enhanced MRI are the gold standard in HCC diagnosis [4]. Lesions are typically hypervascular in the hepatic arterial phase, with washout and rim

enhancement in the venous/delayed phases [4]. Liver-specific contrast agents like gadoxetate disodium (Gd-EOB-DTPA) can be added to conventional MR imaging, which helps to better visualize liver vasculature and assess data regarding hepatocytes function. These features of Gd-EOB-DTPA have resulted in improved accuracy in HCC diagnosis, as compared to other MRI techniques and dynamic contrast-enhanced computed tomography [5]. Additionally, new advancements in imaging technology have provided opportunities to investigate the microenvironment of tumors. Methods like dynamic contrast-enhanced (DCE) MRI and diffusion-weighted imaging (DWI) facilitated the accurate examination of tumors' metabolism and proliferation [6]. DWI can provide information regarding tissue cellularity, necrosis, and cell membrane integrity [7]. On the other hand, Gadoteric acid is a liver-specific contrast agent that has been regularly used in liver MRI scans and emerged as an important tool for HCC diagnosis [8]. Published data regarding the role of DWI and DCE-MRI in prediction of tumor grade and/or microvascular environment in HCC were inconsistent. In addition, while mean apparent diffusion coefficient (ADC) values are typically used, others have suggested the use of minimum ADC or true diffusion as possible measures. Similarly, in the use of DCE-MRI, both quantitative and semi-quantitative parameters have been explored [9–12]. New developments in the field of artificial intelligence (AI) and machine learning have made it possible to use analytical algorithms to extract a large number of features from imaging data [13]. The use of radiomics may help build more accurate and reproducible results and additionally has the potential to provide new information regarding tumors' texture and other characteristics [14]. Radiomics has been performed in a variety of imaging sequences for tumor differentiation and grading, including T1-weighted images, T2-weighted images, ADC maps, DCE maps, and T1 maps [15–18]. In this study, we aimed to use radiomics on imaging data from volumetric ADC and volumetric venous enhancement maps to predict the histopathologic degree of differentiation in HCC tumors.

2. Materials and Methods

2.1. Study Population

This was a monocentric, retrospective study compliant with Health Insurance Portability and Accountability Act (HIPAA) policies. Informed patient consent was waived by our Institutional Review Board (IRB). Inclusion criteria are shown in Figure 1. A total of 129 HCC patients with baseline MRI and pathologic report were identified between January 2003 and June 2017. All lesions were hypervascular on hepatic arterial phase imaging, with washout on portal venous/delayed phases and rim enhancement.

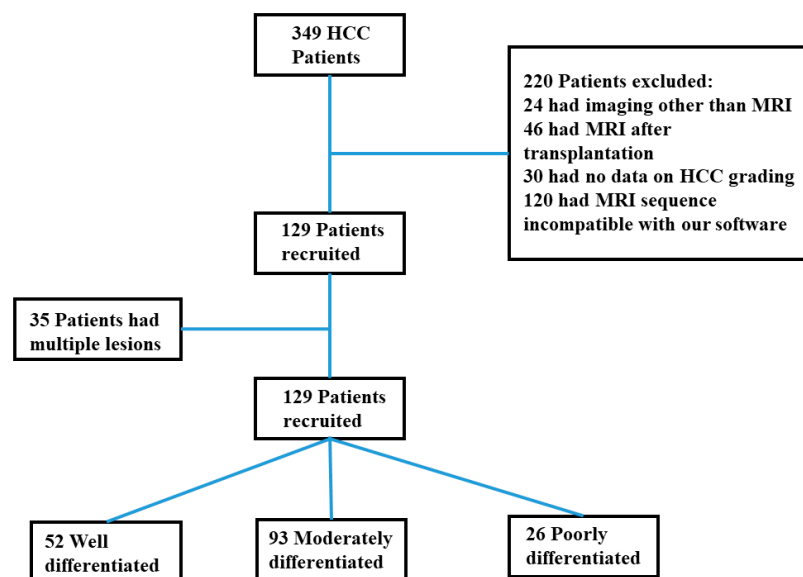


Figure 1. Flowchart shows initial study population, patients excluded, and final study population.

2.2. Histopathology

All sample tissues were obtained following transplantation, resection, or biopsy of the liver and stained with Hematoxylin-eosin. A pathology resident evaluated all tissue samples, and the findings were confirmed by an attending pathologist. Both pathologists were blinded to the MRI findings. Tumor differentiation was defined as well, moderately, or poorly differentiated based on Edmondson–Steiner’s system [19] and using the most dominant grading among the specimens.

2.3. MRI Technique and Tumor Segmentation

Our standard protocol was used to perform MR imaging, as shown in Table 1.

Table 1. MR scanning protocol parameters.

| Parameters | T1WI | T2WI | DWI | DKI | T2*WI |
|------------------------------|---------------|-------------------------------------|---------------|---------------|--|
| Sequence | FSE | FSE | SS-EPI | SS-EPI | Multiecho GRE |
| Orientation | Oblique axial | Oblique axial, sagittal and coronal | Oblique axial | Oblique axial | Oblique axial |
| Repetition time (msec) | 500 | 5629 | 4000 | 3000 | 100 |
| Echo time (msec) | 75 | 85 | 75 | 75 | 2.7, 6.8, 10.9, 15.1, 19.2, 23.3, 27.4, 31.5, 35.6, 39.7, 43.8, 48.0, 52.1 |
| FOV (mm ²) | 380 × 380 | 200 × 200 | 400 × 400 | 360 × 252 | 240 × 192 |
| Matrix (mm ²) | 320 × 224 | 448 × 314 | 160 × 128 | 128 × 128 | 192 × 160 |
| Slice Thickness (mm) | 5 | 3 | 3 | 3 | 3 |
| Slice Gap (mm) | 1 | 0 | 0 | 0 | 0 |
| NEX | 2 | 4 | 12 | 2 | 1 |
| b-value (s/mm ²) | N/A | N/A | 0, 800 | 0, 1000, 2000 | N/A |
| Bandwidth (kHz) | 62.50 | 31.3 | 250 | 250 | 31.3 |
| Scan time | 1 min 44 s | 4 min 4 s | 2 min 32 s | 5 min 9 s | 1 min 22 s |

GRE = gradient-recalled echo; SS-EPI = single-shot echo planar imaging; FSE = Fast spin-echo; FOV = field-of-view; NEX = number of excitations.

Tumor segmentation was performed as reported in prior studies (Appendix A).

Up to 4 dominant lesions in each patient were segmented using semi-automated “Random-Walker” 3D algorithm on portal venous phase (PVP) images by a postdoctoral fellow (—) with >2 years of experience in using the software, who was blinded to pathology results. Then target tumor, histograms, and volumetric statistics were obtained for volumetric ADC and VE (vADC and vVE) parameters [20,21].

2.4. Feature Extraction

An in-house-developed MATLAB-based (R2017b, Mathworks Inc., Natick, MA, USA) program was used to perform analysis using the texture analysis toolbox (<https://github.com/mvallieres/radiomics>, accessed on 12 August 2021), which extracted 95 texture features from the segmented tumor (Figure 2).

The analysis included 9 global features, in addition to 43 features each for ADC and VE maps: 3 histogram-based features, 9 gray-level co-occurrence matrix features (GLCM), 13 gray-level run-length matrix features (GLRLM), 13 gray-level size-zone matrix (GLSZM) features, and 5 neighborhood gray-tone difference matrix (NGTDM) features.

Global features included the mean, maximum, and minimum voxel intensity for both ADC and VE maps. In addition to the 6 global features above, ADC-map derived tumor solidity, surface area, and volume were also included. The texture analysis consisted of the following histogram-based features: Variance, skewness, and kurtosis. Histogram-based features, unlike all other texture features, were spatially invariant such that the arrangement of the pixels relative to one another did not affect the analysis.

The GLCM, GLRLM, GLSZM, and NGTDM matrix features included are shown in Table 2.

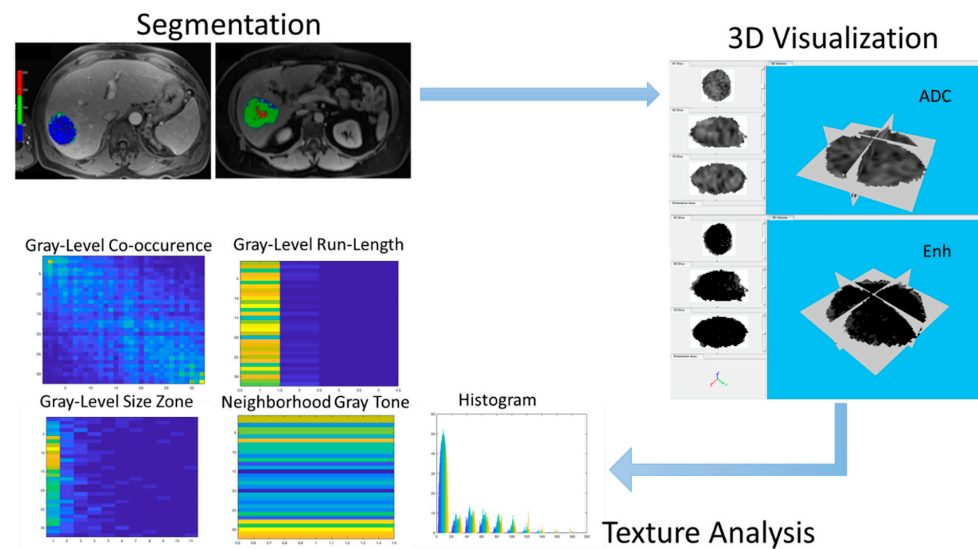


Figure 2. The overall schematic showing tumor radiomics from segmentation to 3D visualization to radiomics on gray-level 3D tumors.

Table 2. Extracted Texture Features from the Tumor Segments.

| Texture Feature Category | Extracted Features in Each Category |
|---|---|
| Global Features | Mean, Maximum, and Minimum (for both ADC and VE), Tumor Solidity, Surface Area, and Volume |
| Histogram-based Features | Variance, Skewness, and Kurtosis |
| Gray Level Co-occurrence Matrix Features (GLCM) * | Contrast, Correlation, Energy, Variance, Sum average, Dissimilarity, Autocorrelation, Entropy, and Homogeneity |
| Gray Level Run Length Matrix Features (GLRLM) ** | Short-run emphasis (SRE), Long-run Emphasis (LRE), Gray-level non-uniformity (GLN), Run-length non-uniformity (RLN), Run Percentage (RP), Low Gray-level Run Emphasis (LGRE), High Gray-level Run Emphasis (HGRE), Short Run Low Gray-level Emphasis (SRLGE), Short Run High Gray-level Emphasis (SRHGE), Long Run Low Gray-level Emphasis (LRLGE), Long Run High Gray-level Emphasis (LRHGE), Gray-level Variance (GLV), and Run Length Variance (RLV) |
| Gray Level Size Zone Matrix Features (GLSZM) *** | Small Zone Emphasis (SZE), Large Zone Emphasis (LZE), Gray-level non-uniformity (GLN), Zone Size non-uniformity (ZSN), Zone percentage (ZP), Low Gray-level Zone Emphasis (LGZE), High Gray-level Zone Emphasis (HGZE), Small Zone Low Gray-level Emphasis (SZHGE), Large Zone Low Gray-level Emphasis (LZLGE), Large Zone High Gray-level Emphasis (LZHGE), Gray-level Variance (GLV), and Zone Size Variance (RLV) |
| Neighborhood Gray-tone Difference Matrix (NGTDM) **** | Mean, Variance, Kurtosis, Strength, and Skewness |

* GLCM elements in row (i) and column (j) represent the frequency in which a given gray level of value (i) is horizontally adjacent to gray-level (j). For the purposes of this study, these calculations were performed in vertical, horizontal, 45°, and 135° directions, which were then averaged together to minimize directional dependence in the samples.

** Rows (i) represent the gray-levels while the columns (j) represent the run-length, or the consecutive number of pixels with a particular gray-level. Elements within the matrix represent the frequency of pixel line segments with a run-length (j) and a gray-level (i).

*** Rows (i) represent the gray-levels while the columns (j) represent the 3D zone-size, or the consecutive number of 3D zones with a particular gray-level. Elements within the matrix represent the frequency of zones with a zone-size (j) and a gray-level (i).

**** these features provide a histogram of the absolute gradient values in the tissue segment. In this analysis, differences in all pixel values within a tumor segment were analyzed using a 3×3 neighborhood

GLCM features were calculated based on a symmetric matrix with rows (i) and columns (j) ranging from 0 to Ng, such that Ng is equal to the number of gray-levels within the image.

2.5. Grey Level Discretization

To investigate the dependence of texture features on the number of gray levels (Ng), texture features were extracted with resampled Ng values of 16, 32, 64, 128, and 256. Of these, 64 was the optimal value in our analysis and provided the best classification performance.

2.6. Statistical Analysis

In our analysis, we compare the ability of radiomics to classify tumor differentiation compared to the mean ADC and venous enhancement values alone. Once the features were extracted using texture analysis, statistical machine learning was used to identify the performance of the combined set of texture features in the classification of tumors into well, moderately, and poorly differentiated classes. We used both a two-class (well vs. moderate/poor) and a multi-class (well vs. moderate vs. poor) random forest classification algorithm [22] for that purpose and then tuned the algorithm to optimize the parameters. The Gini index was used for split criterion. Parameters used in the multi-class classification were: Minimum leaf node size = 9, number of variables tried at each split = 44, and number of decision trees = 500. Predictor importance was estimated based on the minimal depth of the maximal subtree. If a predictor is influential in prediction, then the variable is likely to occur nearer to the root rather than the leaf nodes. The out-of-bag error from the random forest algorithm was used as the metric to quantify classification error and assess performance (Figure 3).

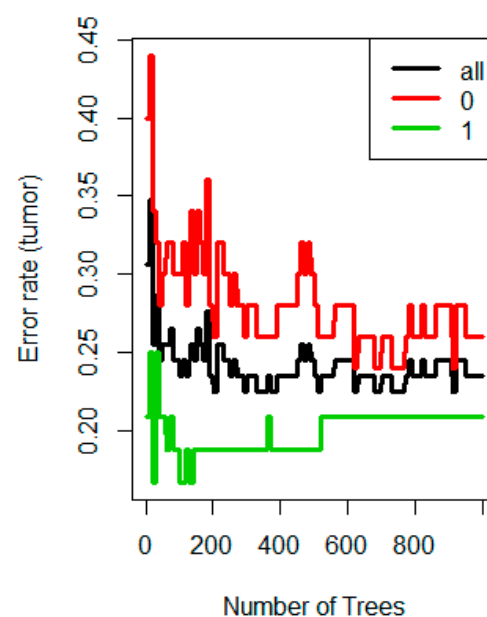


Figure 3. The effect of increasing the number of trees used for building the forest. The out-of-bag error rate stabilizes after around 400 trees in our study.

OOB estimates measure the prediction error of random forest models utilizing bootstrap aggregating (bagging). Bagging uses subsampling with replacement to create training samples for the model to learn from. Bootstrap aggregating allows one to define an out-of-bag estimate of the prediction performance improvement by evaluating predictions on those observations which were not used in the building of the base learner. The ability of the model to distinguish well from moderate/poorly differentiated tumors was quantified using the area under the receiver operating characteristic (ROC) curve (AUC) and misclassification error rates. OOB AUC's between the models were compared to assess if the differences in AUC were significant (pROC package). A chi-squared test was used to compare if the differences in the OOB misclassification rates were significant.

Stata software (Version 15, StataCorp, College Station, TX, USA) was used for the analysis of demographic and clinical parameters. Normality of these variables was assessed by Shapiro–Wilk test, and appropriate statistical tests were used for univariate associations. Kruskal–Wallis and Chi square tests were used for continuous and categorical parameters, respectively. All p -values were considered statistically significant at $p < 0.05$.

3. Results

3.1. Descriptive Findings

A total of 171 HCC lesions were assessed in 129 patients. The median time between MRI and biopsy was 30 days (range 12–68 days). The median time between MRI and resection/transplantation was 191 days (range 93–316 days). All demographic characteristics (Age, Sex, Race) were similar between well, moderate, and poorly differentiated groups. There was no significant difference in patients' Child scores between the three groups. There was no correlation between lesion location and its degree of differentiation. Alpha-Fetoprotein (AFP) was significantly higher in poorly differentiated HCCs as compared to well and moderately differentiated HCCs ($p = 0.003$). Table 3 summarizes the demographic and clinical characteristics of all patients.

Table 3. Demographic and clinical parameters in all HCC patients, and in subgroups of well, moderately, and poorly differentiated histopathology.

| Parameter | | Total | Degree of Differentiation | | | p Value $^{\Delta}$ |
|---------------------------|------------|----------------------|---------------------------|--------------|----------------------|-----------------------|
| | | | Well | Moderate | Poor | |
| Age *, years | | 62 (57–68) | 61 (57–69) | 62 (58–66) | 63 (57–73) | 0.68 |
| Sex, n (%) | Male | 102 (79%) | 28 (21.7%) | 60 (46.5%) | 14 (10.8%) | 0.35 |
| | Female | 27 (20.9%) | 11 (8.5%) | 12 (9.3%) | 4 (3.1%) | |
| Race, n (%) | White | 72 (55.8%) | 18 (13.9%) | 40 (31%) | 14 (10.8%) | 0.40 |
| | Black | 35 (27.1%) | 12 (9.3%) | 20 (15.5%) | 3 (2.3%) | |
| | Asian | 9 (6.9%) | 4 (3.1%) | 4 (3.1%) | 1 (0.70%) | |
| | Other | 13 (10%) | 5 (3.8%) | 8 (6.2%) | 0 (0%) | |
| Child-Pugh score, n (%) | Child A | 91 (70.5%) | 31 (24%) | 45 (34.8%) | 15 (11.6%) | 0.12 |
| | Child B | 33 (25.5%) | 8 (6.2%) | 22 (17%) | 3 (2.3%) | |
| | Child C | 5 (3.8%) | 0 (0%) | 5 (3.8%) | 0 (0%) | |
| Patients' outcome, n (%) | Alive | 71 (55%) | 25 (19.3%) | 39 (30.2%) | 7 (5.4%) | 0.12 |
| | Died | 52 (40.3%) | 12 (9.3%) | 29 (22.4%) | 11 (8.5%) | |
| Lobe, n (%) ‡ | Left | 41 (31.7%) | 16 (12.4%) | 19 (14.7%) | 6 (4.6%) | 0.26 |
| | Right | 84 (65.1%) | 23 (17.8%) | 49 (37.9%) | 12 (9.3%) | |
| | Both lobes | 4 (3.1%) | 0 (0%) | 4 (3.1%) | 0 (0%) | |
| AFP *, ng/mL | | 22.5 (6.8–171.93) | 9.2 (4–94) | 22 (7.8–125) | 256.3 (36.3–9621) | 0.003 |

AFP: alpha fetoprotein

* All continuous variables are presented by their median and (interquartile ranges)

‡ Total number of lesions is more than the number of patients. More than 1 lesion was identified in 35 patients.

$^{\Delta}$ p Values of Kruskal–Wallis test reported for continuous variables (age, AFP), and P values of chi square test reported for categorical parameters (sex, race, Child–Pugh score, patients' outcome, lobe)

3.2. Radiomics Feature Extraction

Of the total of 95 texture features that were extracted, ADC features performed better in distinguishing well differentiated from poorly differentiated HCCs. The top radiomics

features estimated from the minimum depth of the maximal subtree for the multi-class random forest classifier were also extracted (Figure 4). Top features as obtained from the multi-class classification algorithm were as follows: (1) Mean ADC value, (2) ADC gray-level zone-length matrix low gray level zone emphasis, (3) enhancement NGTDM coarseness, (4) ADC global variance, and (5) ADC gray-level zone-length matrix short zone low gray level emphasis.

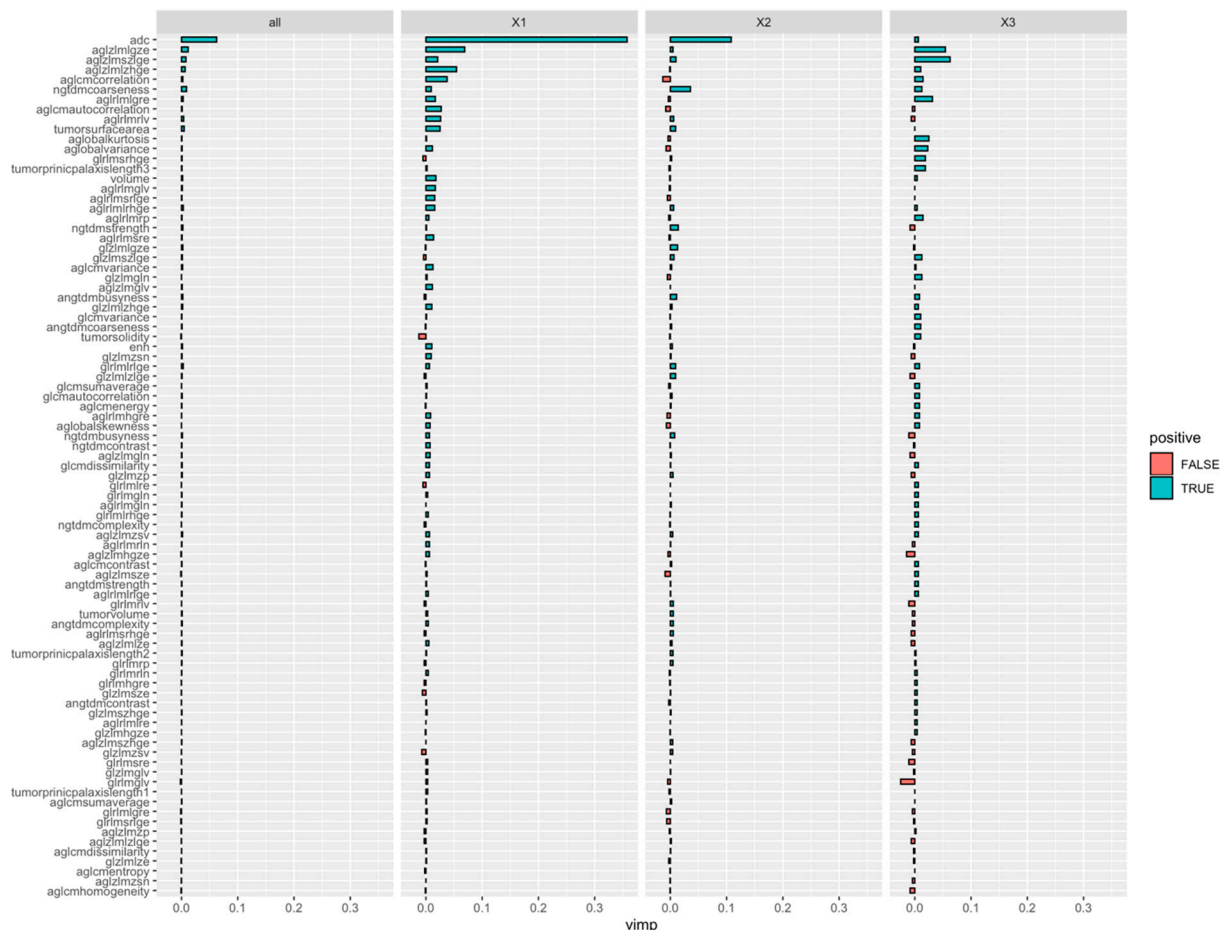


Figure 4. A variable importance plot showing that while mean ADC effectively differentiates well (X1) from moderate (X2) and poor (X3), the addition of radiomics features is particularly helpful in improved differentiation between moderate and poor categories.

3.3. Classification Ability of Radiomics-Based Model

The mean ADC and venous enhancement map alone had an out-of-bag error rate of 39.8%, the error decreased to 32.8% ($p < 0.01$) with the addition of the radiomics features in the multi-class model.

The AUC improved significantly from 75.2% to 83.2% ($p = 0.03$) with the addition of the radiomics features for distinguishing well differentiated from moderate/poorly differentiated HCCs in the multi-class model (Figure 5).

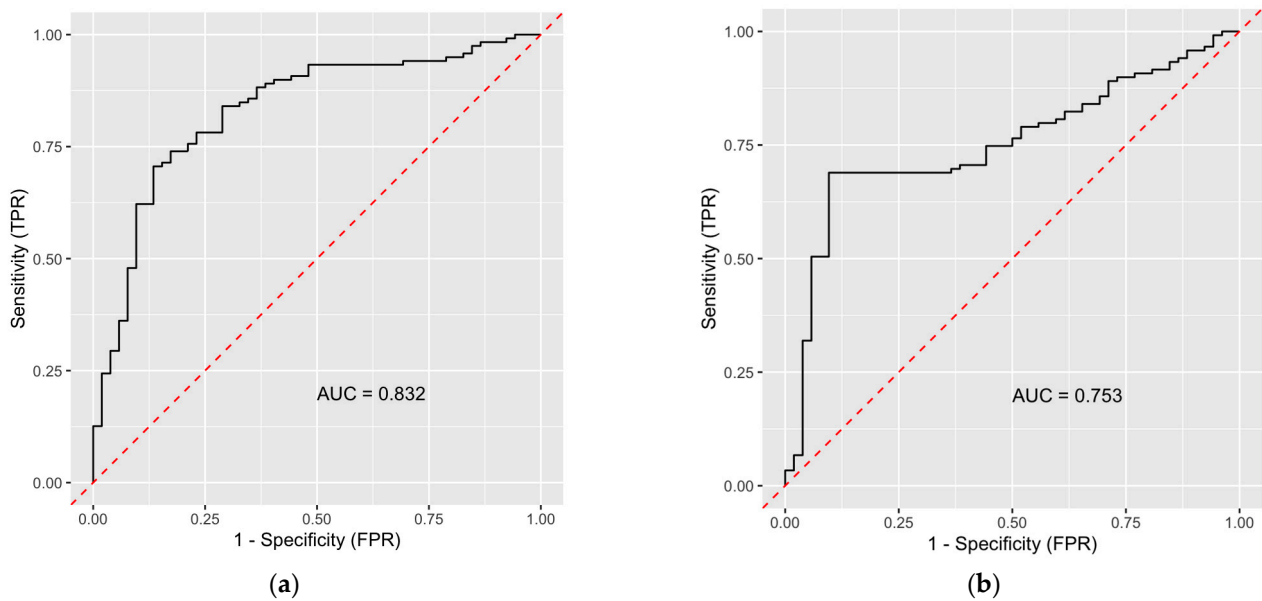


Figure 5. ROC curves showing the performance of models for classifying well from moderate/poorly differentiated tumors with (a) and without (b) radiomics-derived texture features in the multi-class model.

In the two-class problem, the addition of radiomics features decreased the overall error rate from 27.5% to 22.2% ($p < 0.01$) and increased the AUC from 77.9% to 81.5% ($p = 0.18$). (Figure 6).

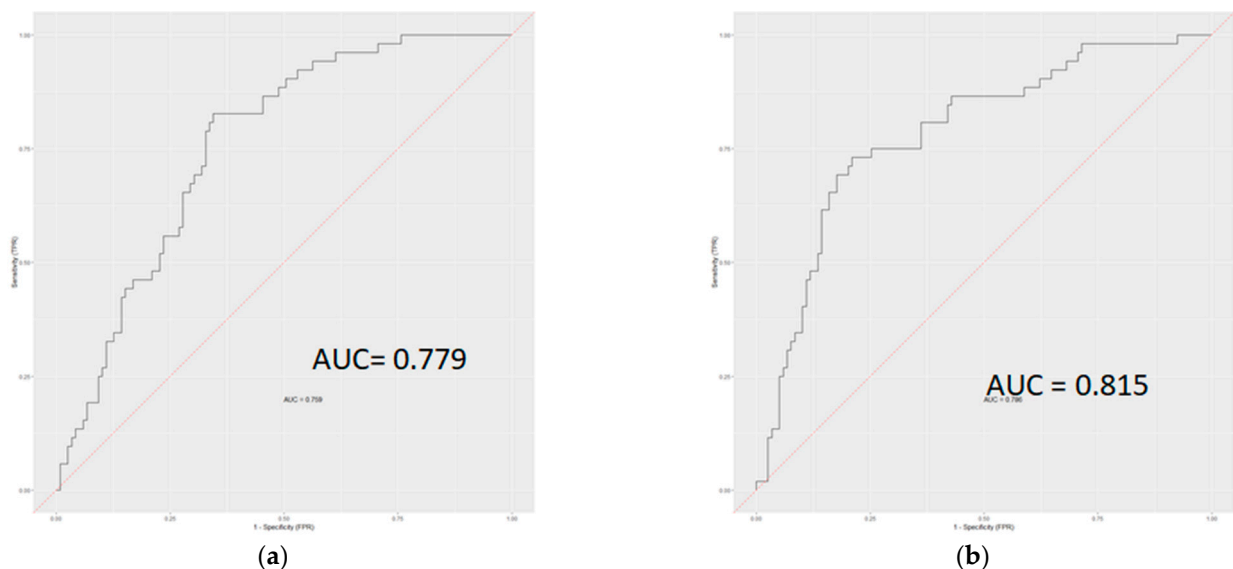


Figure 6. ROC curves showing the performance of models for classifying well from moderate/poorly differentiated tumors without (a) and with (b) radiomics-derived texture features in the two-class model.

4. Discussion

In this study, we used a radiomics framework that included texture extraction followed by statistical machine learning to analyze the role of volumetric ADC and venous enhancement maps in determining the histopathology of HCC. Using a random forest classification algorithm, we demonstrated that ADC radiomics features were among the top classifiers in variable importance ranking for classifying HCC tumors as compared to VE features. From all the features, we identified five that were superior to other features in

tumor classification. The addition of radiomics textures improved classification compared to ADC or venous enhancement values alone, indicating a potential role for radiomics in non-invasive histologic grading of HCC tumors.

To date, despite the major improvement in surgical and chemotherapy techniques, survival of HCC patients remains poor. High recurrence rate is among the main reasons for poor survival in treated patients [23]. Poorly differentiated HCCs have been reported to have higher recurrence rates as compared to well and moderately differentiated tumors and with worse overall survival [2]. Poorly differentiated HCCs need more extensive resection in order to reduce the recurrence rate after surgery [24]. Additionally, more frequent follow-ups might be needed in poorly differentiated HCCs for early detection of recurrence and metastasis [25]. Fine-needle aspiration (FNA) biopsy is the pre-operative gold standard in determining histopathological grading of HCC. However, it is an expensive and invasive method with an increased risk of adverse outcomes, including bleeding, tumor seeding, and sampling errors [26]. Due to the heterogeneous nature of HCC, tissue samples provided by biopsy might not be a good representative of the entire tumor. Therefore, identifying a non-invasive and accurate method to assess tissue characteristics of tumors can be of great importance.

The radiomics' potential role has been studied for predicting treatment response, recurrence, and overall survival in HCC patients [27,28]. Additionally, several studies have exploited radiomics on pre-contrast T1-W, post-contrast T1-W, T2W MRI, and also contrast-enhanced computed tomography (CE-CT) imaging to distinguish between well differentiated and moderately/poorly differentiated HCC [18,29,30]. Zhang et al. [31] used DWI radiomics features in combination with T1- and T2-weighted imaging to predict microvascular invasion (MVI) in HCC. Their results showed that radiomics features can classify MVI HCCs and non-MVI HCCs with an accuracy of 78% in the training cohort and 82% in the validation cohort.

The results of a study by Hectors et al. showed no association between ADC radiomics features and degree of tumor differentiation of HCCs [32]. In their study, they placed an ROI on the HCC tumor on a single slice of the ADC map. Therefore, the results might not be representative of the whole tumor.

Another study done by Zhou et al. used a convolutional neural network to extract deep features from log maps resulting from three-b-value images of DWI. Their results showed higher performance of their model for HCC grading as compared to ADC maps [26]. Gadolinium-based contrast agents have been used previously in differentiating HCC from benign lesions [33], and studies showed inconclusive results regarding their role in distinguishing HCC histopathological grading [34,35]. With the use of machine learning, several studies exploited contrast-enhanced imaging in predicting early and late recurrence in HCC patients [36,37].

We exploited random forest (RF) classifiers in our study as the machine learning algorithm of choice. RFs have several inherent advantages over other classifiers like statistical logistic regression techniques that are routinely used: (1) They deal well with non-linear associations as the tree method identifies several cut-points during branching, (2) the variables do not have to be normally distributed, (3) the algorithm provides added robustness to prevent overfitting by randomly choosing a subset of variables at each node and also choosing a subset of patient data for each tree, and (4) the algorithm also provides the importance of each variable used.

There were some limitations to our study. First, this study was retrospective, and patients' data were recorded for several years. The variation in study setting over time is an inherent limitation to all retrospective studies. This limitation was minimized by adhering to consistent protocols in our institute. The other limitation is the use of either biopsy or the entire tumor examination for histopathology grading. This could have potentially affected our findings as the accuracy of biopsy might be lower than tumor excision. However, we performed subgroup analysis in these two groups and also adjusted our final multivariable models for the sampling method, which demonstrated consistent

results. Future prospective studies with a better control of confounders can determine other predictors of tumor grading and patients' survival.

In conclusion, the addition of radiomics-based texture analysis improved classification over and above that of ADC or venous enhancement values alone. Radiomics, by better capturing the tumor microenvironment, may assist in non-invasive histologic grading of HCC tumors.

Author Contributions: S.A.: Primary author, manuscript preparation, editing and submission. B.A.V.: Advanced statistical analysis and machine learning techniques. M.S.: Manual demographic data extraction. M.G.: Image review and tumor segmentation. B.H.: Image review and tumor segmentation. R.R.H.: Image review and tumor segmentation. M.A.G.: Histogram analysis, statistical analysis and pathology review. P.K.: Histogram analysis, statistical analysis and pathology review. A.P.: Histogram analysis, statistical analysis and pathology review. P.P.: Statistical analysis and pathology review. L.P.: Software optimization and postprocessing troubleshooting. R.G.: Software optimization and postprocessing troubleshooting. I.R.K.: Data integrity and oversight of the entire project. All authors have read and agreed to the published version of the manuscript.

Funding: This research received no external funding.

Institutional Review Board Statement: The study was conducted in accordance with the Declaration of Helsinki, and approved by the Institutional Review Board (or Ethics Committee) of Johns Hopkins Hospital (protocol code NA 00002111).

Informed Consent Statement: Informed patient consent was waived by our Institutional Review Board (IRB).

Data Availability Statement: Data available upon request, please contact Corresponding Author.

Conflicts of Interest: The authors declare no conflict of interest.

Appendix A

Appendix A.1. MRI Technique

Our standard protocol was used on a 1.5 T MRI scanner (Siemens MAGNETOM Avanto, Siemens Healthineers, Erlangen, Germany) equipped with a phased-array body coil to perform MR imaging on our patients [38]. This included T2-weighted turbo spin-echo images (matrix size, 256×256 ; slice thickness, 8 mm; interslice gap, 2 mm; repetition time [TR]/echo time [TE] 4500/92 ms; receiver bandwidth, 32 kHz) and breath-hold DWI single-shot echo-planar images (matrix size, 128×128 ; slice thickness, 8 mm; interslice gap, 2 mm; b-value = 50 and 750 s/mm²; TR 3000 ms; TE 69 ms; receiver bandwidth, 64 kHz). We also obtained breath-hold unenhanced and contrast-enhanced (0.1 mmol/kg intravenous gadopentetate dimeglumine [Magnevist, Bayer Healthcare, Leverkusen, Germany]; injection rate 2 cc/s) T1-weighted 3D fat-suppressed spoiled-gradient-echo images (field of view, 320–400 mm²; matrix size, 192×160 ; slice thickness, 2.5 mm; TR 5.77 ms; TE, 2.77 ms; receiver bandwidth, 64 kHz; flip angle, 10°), in the arterial (20 s), portal (70 s), and delayed (3 min) phases.

Appendix A.2. Segmentation

From all sequences of contrast-enhanced MR imaging, DWI, ADC maps, pre-contrast T1-weighted images, and portal venous phase (PVP) images (T1-weighted images at 70 s) were selected and retrieved as digital imaging and communications in medicine (DICOM) format from our picture archiving and communicating system (PACS, Carestream, Rochester, NY, USA) and anonymized.

Primarily, the pre-contrast (P) and portal venous phase (PVP) images were transferred to a prototype software (MR Arithmetics, Siemens Healthineers, Erlangen, Germany). Then, P images were aligned to PVP images using a non-rigid (deformable) 3D registration method to improve the capture range and accuracy. Then the portal venous enhancement map was calculated as $VE = (PVP - P) / P \times 100$ and exported in DICOM format. These results were reported as relative intensity ratio (RIR), which showed the increase in signal

intensity during the portal phase relative to the pre-contrast phase and are an estimate of accumulated contrast agent in tumor cells.

Then the PVP image, the previously computed VE map, the lowest acquired b-value ($b = 50 \text{ s/mm}^2$), and the ADC map were loaded into a prototype software (MR Multi-parametric Analysis, Siemens Healthineers, Erlangen, Germany) for segmentation. The low-b-value images with high anatomic detail were elastically co-registered to the PVP images to ensure accurate anatomic alignment of images, and the resulting transformation was also applied to the ADC map, which was calculated based on both b-values [39,40].

Up to four dominant lesions in each patient were selected. A semi-automated “Random Walker” 3D segmentation algorithm was used to segment the entire lesion of interest on PVP images [20] by a postdoctoral fellow (—) with >2 years of experience in using the software and reading abdominal MRI, who was blinded to pathology results. After semi-automated segmentation of the target tumor, the prototype software automatically reconstructed the tumor in three dimensions and generated the histograms and volumetric statistics as volumetric ADC and VE (vADC and vVE) parameters [21].

References

1. Torre, L.A.; Bray, F.; Siegel, R.L.; Ferlay, J.; Lortet-Tieulent, J.; Jemal, A. Global cancer statistics, 2012. *CA Cancer J. Clin.* **2015**, *65*, 87–108. [\[CrossRef\]](#)
2. Han, D.H.; Choi, G.H.; Kim, K.S.; Choi, J.S.; Park, Y.N.; Kim, S.U.; Park, J.Y.; Ahn, S.H.; Han, K.-H. Prognostic significance of the worst grade in hepatocellular carcinoma with heterogeneous histologic grades of differentiation. *J. Gastroenterol. Hepatol.* **2013**, *28*, 1384–1390. [\[CrossRef\]](#)
3. Li, X.; Zhang, K.; Shi, Y.; Wang, F.; Meng, X. Correlations between the minimum and mean apparent diffusion coefficient values of hepatocellular carcinoma and tumor grade. *J. Magn. Reson. Imaging* **2016**, *44*, 1442–1447. [\[CrossRef\]](#) [\[PubMed\]](#)
4. Kitao, A.; Zen, Y.; Matsui, O.; Gabata, T.; Kobayashi, S.; Koda, W.; Kozaka, K.; Yoneda, N.; Yamashita, T.; Kaneko, S.; et al. Hepatocellular Carcinoma: Signal Intensity at Gadoteric Acid-enhanced MR Imaging—Correlation with Molecular Transporters and Histopathologic Features. *Radiology* **2010**, *256*, 817–826. [\[CrossRef\]](#)
5. Chou, Y.-C.; Lao, I.-H.; Hsieh, P.-L.; Su, Y.-Y.; Mak, C.-W.; Sun, D.-P.; Sheu, M.-J.; Kuo, H.-T.; Chen, T.-J.; Ho, C.-H.; et al. Gadoteric acid-enhanced magnetic resonance imaging can predict the pathologic stage of solitary hepatocellular carcinoma. *World J. Gastroenterol.* **2019**, *25*, 2636–2649. [\[CrossRef\]](#)
6. Colen, R.R.; Wang, J.; Singh, S.K.; Gutman, D.A.; Zinn, P.O. Glioblastoma: Imaging Genomic Mapping Reveals Sex-specific Oncogenic Associations of Cell Death. *Radiology* **2015**, *275*, 215–227. [\[CrossRef\]](#)
7. Kele, P.G.; van der Jagt, E.J. Diffusion weighted imaging in the liver. *World J. Gastroenterol.* **2010**, *16*, 1567–1576. [\[CrossRef\]](#)
8. Saito, K.; Kotake, F.; Ito, N.; Ozuki, T.; Mikami, R.; Abe, K.; Shimazaki, Y. Gd-EOB-DTPA Enhanced MRI for Hepatocellular Carcinoma: Quantitative Evaluation of Tumor Enhancement in Hepatobiliary Phase. *Magn. Reson. Med. Sci.* **2005**, *4*, 1–9. [\[CrossRef\]](#)
9. Park, I.K.; Yu, J.-S.; Cho, E.-S.; Kim, J.H.; Chung, J.-J. Apparent diffusion coefficient of hepatocellular carcinoma on diffusion-weighted imaging: Histopathologic tumor grade versus arterial vascularity during dynamic magnetic resonance imaging. *PLoS ONE* **2018**, *13*, e0197070. [\[CrossRef\]](#)
10. Surov, A.; Pech, M.; Omari, J.; Fischbach, F.; Damm, R.; Fischbach, K.; Powerski, M.; Relja, B.; Wienke, A. Diffusion-Weighted Imaging Reflects Tumor Grading and Microvascular Invasion in Hepatocellular Carcinoma. *Liver Cancer* **2021**, *10*, 10–24. [\[CrossRef\]](#)
11. Li, J.; Xue, F.; Xu, X.; Wang, Q.; Zhang, X. Dynamic contrast-enhanced MRI differentiates hepatocellular carcinoma from hepatic metastasis of rectal cancer by extracting pharmacokinetic parameters and radiomic features. *Exp. Ther. Med.* **2020**, *20*, 3643–3652. [\[CrossRef\]](#)
12. Chen, J.; Si, Y.; Zhao, K.; Shi, X.; Bi, W.; Liu, S.-E.; Hua, H. Evaluation of quantitative parameters of dynamic contrast-enhanced magnetic resonance imaging in qualitative diagnosis of hepatic masses. *BMC Med. Imaging* **2018**, *18*, 56. [\[CrossRef\]](#)
13. Aerts, H.J.W.L.; Velazquez, E.R.; Leijenaar, R.T.H.; Parmar, C.; Grossmann, P.; Carvalho, S.; Bussink, J.; Monshouwer, R.; Haibe-Kains, B.; Rietveld, D.; et al. Decoding tumour phenotype by noninvasive imaging using a quantitative radiomics approach. *Nat. Commun.* **2014**, *5*, 4006. [\[CrossRef\]](#)
14. Gillies, R.J.; Kinahan, P.E.; Hricak, H. Radiomics: Images Are More than Pictures, They Are Data. *Radiology* **2016**, *278*, 563–577. [\[CrossRef\]](#)
15. Wang, L.; Zhang, L.; Jiang, B.; Zhao, K.; Zhang, Y.; Xie, X. Clinical application of deep learning and radiomics in hepatic disease imaging: A systematic scoping review. *Br. J. Radiol.* **2022**, *95*, 20211136. [\[CrossRef\]](#)
16. Ren, S.; Qi, Q.; Liu, S.; Duan, S.; Mao, B.; Chang, Z.; Zhang, Y.; Wang, S.; Zhang, L. Preoperative prediction of pathological grading of hepatocellular carcinoma using machine learning-based ultrasomics: A multicenter study. *Eur. J. Radiol.* **2021**, *143*, 109891. [\[CrossRef\]](#)

17. Chen, W.; Zhang, T.; Xu, L.; Zhao, L.; Liu, H.; Gu, L.R.; Wang, D.Z.; Zhang, M. Radiomics Analysis of Contrast-Enhanced CT for Hepatocellular Carcinoma Grading. *Front. Oncol.* **2021**, *11*, 660509. [\[CrossRef\]](#)
18. Wu, M.; Tan, H.; Gao, F.; Hai, J.; Ning, P.; Chen, J.; Zhu, S.; Wang, M.; Dou, S.; Shi, D. Predicting the grade of hepatocellular carcinoma based on non-contrast-enhanced MRI radiomics signature. *Eur. Radiol.* **2019**, *29*, 2802–2811. [\[CrossRef\]](#)
19. Edmondson, H.A.; Steiner, P.E. Primary carcinoma of the liver. A study of 100 cases among 48,900 necropsies. *Cancer* **1954**, *7*, 462–503. [\[CrossRef\]](#)
20. Grady, L. Random Walks for Image Segmentation. *IEEE Trans. Pattern Anal. Mach. Intell.* **2006**, *28*, 1768–1783. [\[CrossRef\]](#)
21. Ameli, S.; Shaghagh, M.; Ghasabeh, M.A.; Pandey, P.; Hazhirkarzar, B.; Ghadimi, M.; Habibabadi, R.R.; Khoshpouri, P.; Pandey, A.; Anders, R.A.; et al. Role of baseline volumetric functional MRI in predicting histopathologic grade and patients' survival in hepatocellular carcinoma. *Eur. Radiol.* **2020**, *30*, 3748–3758. [\[CrossRef\]](#)
22. Ishwaran, H.; Kogalur, U.B.; Chen, X.; Minn, A.J. Random survival forests for high-dimensional data. *Stat. Anal. Data Min. ASA Data Sci. J.* **2011**, *4*, 115–132. [\[CrossRef\]](#)
23. Poon, R.T.-P.; Fan, S.T.; Lo, C.M.; Liu, C.L.; Wong, J. Long-Term Survival and Pattern of Recurrence After Resection of Small Hepatocellular Carcinoma in Patients with Preserved Liver Function: Implications for a strategy of salvage transplantation. *Ann. Surg.* **2002**, *235*, 373–382. [\[CrossRef\]](#)
24. Shi, M.; Guo, R.; Lin, X.-J.; Zhang, Y.-Q.; Chen, M.-S.; Zhang, C.-Q.; Lau, W.Y.; Li, J.-Q. Partial Hepatectomy With Wide Versus Narrow Resection Margin for Solitary Hepatocellular Carcinoma: A prospective randomized trial. *Ann. Surg.* **2007**, *245*, 36–43. [\[CrossRef\]](#)
25. Huang, K.; Dong, Z.; Cai, H.; Huang, M.; Peng, Z.; Xu, L.; Jia, Y.; Song, C.; Li, Z.-P.; Feng, S.-T. Imaging biomarkers for well and moderate hepatocellular carcinoma: Preoperative magnetic resonance image and histopathological correlation. *BMC Cancer* **2019**, *19*, 364. [\[CrossRef\]](#)
26. Zhou, W.; Wang, G.; Xie, G.; Zhang, L. Grading of hepatocellular carcinoma based on diffusion weighted images with multiple b-values using convolutional neural networks. *Med. Phys.* **2019**, *46*, 3951–3960. [\[CrossRef\]](#)
27. Defour, L.B.; Mulé, S.; Tenenhaus, A.; Piardi, T.; Sommacale, D.; Hoeffel, C.; Thiéfin, G. Hepatocellular carcinoma: CT texture analysis as a predictor of survival after surgical resection. *Eur. Radiol.* **2019**, *29*, 1231–1239. [\[CrossRef\]](#)
28. Chen, S.; Zhu, Y.; Liu, Z.; Liang, C. Texture analysis of baseline multiphasic hepatic computed tomography images for the prognosis of single hepatocellular carcinoma after hepatectomy: A retrospective pilot study. *Eur. J. Radiol.* **2017**, *90*, 198–204. [\[CrossRef\]](#)
29. Zhou, W.; Zhang, L.; Wang, K.; Chen, S.; Wang, G.; Liu, Z.; Liang, C. Malignancy characterization of hepatocellular carcinomas based on texture analysis of contrast-enhanced MR images. *J. Magn. Reson. Imaging* **2017**, *45*, 1476–1484. [\[CrossRef\]](#)
30. Oh, J.; Lee, J.M.; Park, J.; Joo, I.; Yoon, J.H.; Lee, D.H.; Ganeshan, B.; Han, J.K. Hepatocellular Carcinoma: Texture Analysis of Preoperative Computed Tomography Images Can Provide Markers of Tumor Grade and Disease-Free Survival. *Korean J. Radiol.* **2019**, *20*, 569–579. [\[CrossRef\]](#)
31. Zhang, R.; Xu, L.; Wen, X.; Zhang, J.; Yang, P.; Zhang, L.; Xue, X.; Wang, X.; Huang, Q.; Guo, C.; et al. A nomogram based on bi-regional radiomics features from multimodal magnetic resonance imaging for preoperative prediction of microvascular invasion in hepatocellular carcinoma. *Quant. Imaging Med. Surg.* **2019**, *9*, 1503–1515. [\[CrossRef\]](#) [\[PubMed\]](#)
32. Hectors, S.J.; Lewis, S.; Besa, C.; King, M.J.; Said, D.; Putra, J.; Ward, S.; Higashi, T.; Thung, S.; Yao, S.; et al. MRI radiomics features predict immuno-oncological characteristics of hepatocellular carcinoma. *Eur. Radiol.* **2020**, *30*, 3759–3769. [\[CrossRef\]](#) [\[PubMed\]](#)
33. Kwon, H.-J.; Byun, J.H.; Kim, J.Y.; Hong, G.-S.; Won, H.J.; Shin, Y.M.; Kim, P.N. Differentiation of small (≤ 2 cm) hepatocellular carcinomas from small benign nodules in cirrhotic liver on gadoxetic acid-enhanced and diffusion-weighted magnetic resonance images. *Abdom. Imaging* **2015**, *40*, 64–75. [\[CrossRef\]](#) [\[PubMed\]](#)
34. Chang, W.-C.; Chen, R.-C.; Chou, C.-T.; Lin, C.-Y.; Yu, C.-Y.; Liu, C.-H.; Chou, J.-M.; Hsu, H.-H.; Huang, G.-S. Histological grade of hepatocellular carcinoma correlates with arterial enhancement on gadoxetic acid-enhanced and diffusion-weighted MR images. *Gastrointest. Radiol.* **2014**, *39*, 1202–1212. [\[CrossRef\]](#) [\[PubMed\]](#)
35. Choi, J.-Y.; Kim, M.-J.; Park, Y.N.; Lee, J.M.; Yoo, S.K.; Rha, S.Y.; Seok, J.Y. Gadaxetate Disodium-Enhanced Hepatobiliary Phase MRI of Hepatocellular Carcinoma: Correlation With Histological Characteristics. *Am. J. Roentgenol.* **2011**, *197*, 399–405. [\[CrossRef\]](#)
36. Zhang, Z.; Jiang, H.; Chen, J.; Wei, Y.; Cao, L.; Ye, Z.; Li, X.; Ma, L.; Song, B. Hepatocellular carcinoma: Radiomics nomogram on gadoxetic acid-enhanced MR imaging for early postoperative recurrence prediction. *Cancer Imaging* **2019**, *19*, 22. [\[CrossRef\]](#)
37. Kim, S.; Shin, J.; Kim, D.-Y.; Choi, G.H.; Kim, M.-J.; Choi, J.-Y. Radiomics on Gadaxetic Acid-Enhanced Magnetic Resonance Imaging for Prediction of Postoperative Early and Late Recurrence of Single Hepatocellular Carcinoma. *Clin. Cancer Res.* **2019**, *25*, 3847–3855. [\[CrossRef\]](#)

38. Corona-Villalobos, C.P.; Halappa, V.G.; Bonekamp, S.; Eng, J.; Reyes, D.; Cosgrove, D.; Rastegar, N.; Pan, L.; Pawlik, T.M.; Kamel, I.R. Functional Magnetic Resonance Imaging Response of Targeted Tumor Burden and Its Impact on Survival in Patients with Hepatocellular Carcinoma. *Investig. Radiol.* **2015**, *50*, 283–289. [[CrossRef](#)]
39. Pandey, A.; Pandey, P.; Ghasabeh, M.A.; Zarghampour, M.; Khoshpouri, P.; Ameli, S.; Luo, Y.; Kamel, I.R. Baseline Volumetric Multiparametric MRI: Can It Be Used to Predict Survival in Patients with Unresectable Intrahepatic Cholangiocarcinoma Undergoing Transcatheter Arterial Chemoembolization? *Radiology* **2018**, *289*, 843–853. [[CrossRef](#)]
40. Zarghampour, M.; Fouladi, D.F.; Pandey, A.; Ghasabeh, M.A.; Pandey, P.; Varzaneh, F.N.; Khoshpouri, P.; Shao, N.; Pan, L.; Grimm, R.; et al. Utility of volumetric contrast-enhanced and diffusion-weighted MRI in differentiating between common primary hypervascular liver tumors. *J. Magn. Reson. Imaging* **2018**, *48*, 1080–1090. [[CrossRef](#)]